machines

MDPI

Article

Finite Element Random-Vibration Analysis of a Vehicle-Mounted Laser Platform Under Three Road Conditions

Yingqi Xiao [1], Jingang Wang [2], Jialong Chen [1], Haiming Zhao [1,*] and Gang Hu [3,*]

[1] College of Mechanical and Electrical Engineering, Central South University, Changsha 410083, China; xyq6tmiles@163.com (Y.X.); 18867377780@163.com (J.C.)
[2] Sunward Intelligent Special Equipment Co., Ltd., Changsha 410100, China; sunward_wangjg@163.com
[3] School of Mechanical and Transportation Engineering, Changsha University of Science and Technology, Changsha 410114, China
* Correspondence: zhm0097@126.com (H.Z.); hug0760@163.com (G.H.)

Abstract

Road-induced vibration of vehicle-mounted laser platforms is stochastic, and the structural response is influenced by support motion, damping, and connection stiffness. This study combines road measurements with finite element (FE) random-vibration analysis to assess the response of a vehicle-mounted laser platform. Two screw-mounted tri-axial accelerometers measured the excitation at the left-wheel support and the response at the laser-head mount during three repeated runs on each of three roads. The records were sampled at 200 Hz for 33.305 s and processed using 1024-sample Hann-windowed Welch estimates with 50% overlap, corresponding to a frequency resolution of 0.1953125 Hz. A three-level modal mesh study supported the selection of an 8 mm global mesh. The random-vibration solution included 20 modes up to 78.911 Hz, while six selected modes were displayed in post-processing. For the three road conditions, the mean absolute error in the three-axis resultant RMS was approximately 4.85%, and the mean logarithmic PSD correlation coefficient over 0–80 Hz was approximately 0.979. The results support comparative response analysis for the tested configuration. The 2% damping ratio and equivalent support stiffnesses were treated as modeling assumptions, and the single measured input required an equivalent uniform-support excitation model.

Keywords: vehicle-mounted laser platform; finite element response assessment; random vibration; road test; repeatability; power spectral density; mesh sensitivity

1. Introduction

Vehicle-mounted laser and optoelectronic equipment is continuously subjected to broadband vibration generated by road-surface irregularities, vehicle powertrains, and auxiliary equipment during transportation and field operation. For precision measurement equipment such as vehicle-mounted light detection and ranging (LiDAR) systems, such vibration not only excites the supporting structure but may also propagate into the measurement and control chains, thereby degrading operational performance. Field tests by Periu et al. showed that vehicle vibration affects the obstacle-localization accuracy of LiDAR and that appropriate support and stabilization devices can mitigate this effect [1]. Schlager et al. demonstrated a relationship between structural resonances in automotive LiDAR and point-cloud quality [2]. Hua et al. developed a dynamic model of a microelectromechanical-system (MEMS) LiDAR micromirror and showed that external vibration interferes with its motion and control performance [3]. These findings indicate

Check for updates

Received: 12 August 2026
Revised: 14 September 2026
Accepted: 20 September 2026
Published: 21 September 2026

Copyright: © 2026 by the authors. Licensee MDPI, Basel, Switzerland. This article is an open access article distributed under the terms and conditions of the Creative Commons Attribution (CC BY) license.

that a structural dynamic model of a vehicle-mounted laser platform should not merely reproduce the vibration characteristics of the platform itself; more importantly, it should predict the dynamic response at the laser-head mounting location under actual road excitation, thereby providing a reliable basis for subsequent vibration-mitigation design and mounting-layout optimization.

Finite element analysis is widely used to investigate the structural dynamics and vibration responses of complex equipment, but the ability of a model to represent the actual structure must be assessed against experimental evidence. Ewins established a modal-testing framework centered on frequency response functions, natural frequencies, and mode shapes [4]. Mottershead and Friswell subsequently incorporated experimental responses into finite element model updating and developed a systematic framework covering parameter selection, sensitivity analysis, and solution methods [5,6]. ASME V&V 10-2019 treats the comparison between computational results and experimental observations as a central component of validation in computational solid mechanics [7], while Oberkampf and Roy emphasized that validation activities should be aligned with the model's intended use [8]. The modal assurance criterion proposed by Allemang provides a quantitative measure of mode-shape correlation [9]. Natural frequencies and mode shapes are therefore important indicators for examining the overall mass, stiffness, and connection characteristics represented by an FE model. However, when the intended use of the model is to predict response amplitudes at a critical location under broadband random road excitation, modal characteristics alone are insufficient; a calculation-to-experiment comparison at the operating-response level is also required.

For large structures that are difficult to excite artificially, operational vibration data provide a practical basis for dynamic assessment. Reynders reviewed operational modal-analysis and system-identification methods [10], and Peeters and De Roeck described stochastic identification using ambient or operating responses [11]. Under road excitation, FE assessment is complicated by stochastic inputs, spatial differences among support motions, spectral uncertainty, and imperfect knowledge of damping and compliant connections. Welch averaging [12], random-data analysis [13], road-profile PSD descriptions [14], and frequency-domain correlation [15] provide suitable analysis tools when the preprocessing, spectral resolution, uncertainty, and comparison bandwidth are stated clearly.

Recent studies have advanced FE model updating and random-vibration assessment. Model-updating research emphasizes the selection of identifiable parameters and the combined use of modal and response data [16–18]. For correlated multi-point excitation, cross-spectral density, phase, and coherence are needed in addition to auto-PSDs [19]. Road-vehicle studies increasingly combine measured operating inputs with numerical response models [20–22], and field-measurement studies provide detailed accounts of sensor placement, repeated runs, preprocessing, and frequency-transmission metrics [23,24]. Random-vibration analysis has also been applied to vehicle electronics and precision components [25–29]. Building on this work, the present study links repeated road measurements with dynamic mesh sensitivity, FE random-vibration analysis, spectral uncertainty, and response comparison at a laser-head mount.

This study examines a vehicle-mounted laser platform on flat asphalt, consecutive speed bumps, and damaged block-stone pavement. The analysis combines a three-level modal mesh-sensitivity study; a 20-mode random-vibration model; three repeated runs on each road; and axis-specific comparisons of time histories, PSDs, coherence, transmissibility, resonance peaks, and RMS response at the laser-head mounting base. Because excitation was measured at one wheel support, the measured directional auto-PSDs were applied as equivalent common inputs at all supports. The findings therefore apply to the tested

platform, loading state, response location, road conditions, speed range, and 0–80 Hz frequency band under this uniform-support-motion assumption.

2. Materials and Methods

2.1. Platform Structure and Finite Element Model

The vehicle-mounted laser emergency-response platform consists of a welded Q235-steel frame, laser source, power-supply box, laser head, and control system, as shown in Figure 1. A parametric three-dimensional assembly was created in SolidWorks 2021 and imported into ANSYS Mechanical 2023 R1. Non-load-bearing holes, minor process features, chamfers, fillets, coatings, and local weld geometry were omitted, while the primary load-carrying members and mounted-equipment masses were retained. Welded interfaces were represented as bonded connections; bolted equipment interfaces were represented by frictional contact with a coefficient of 0.3.

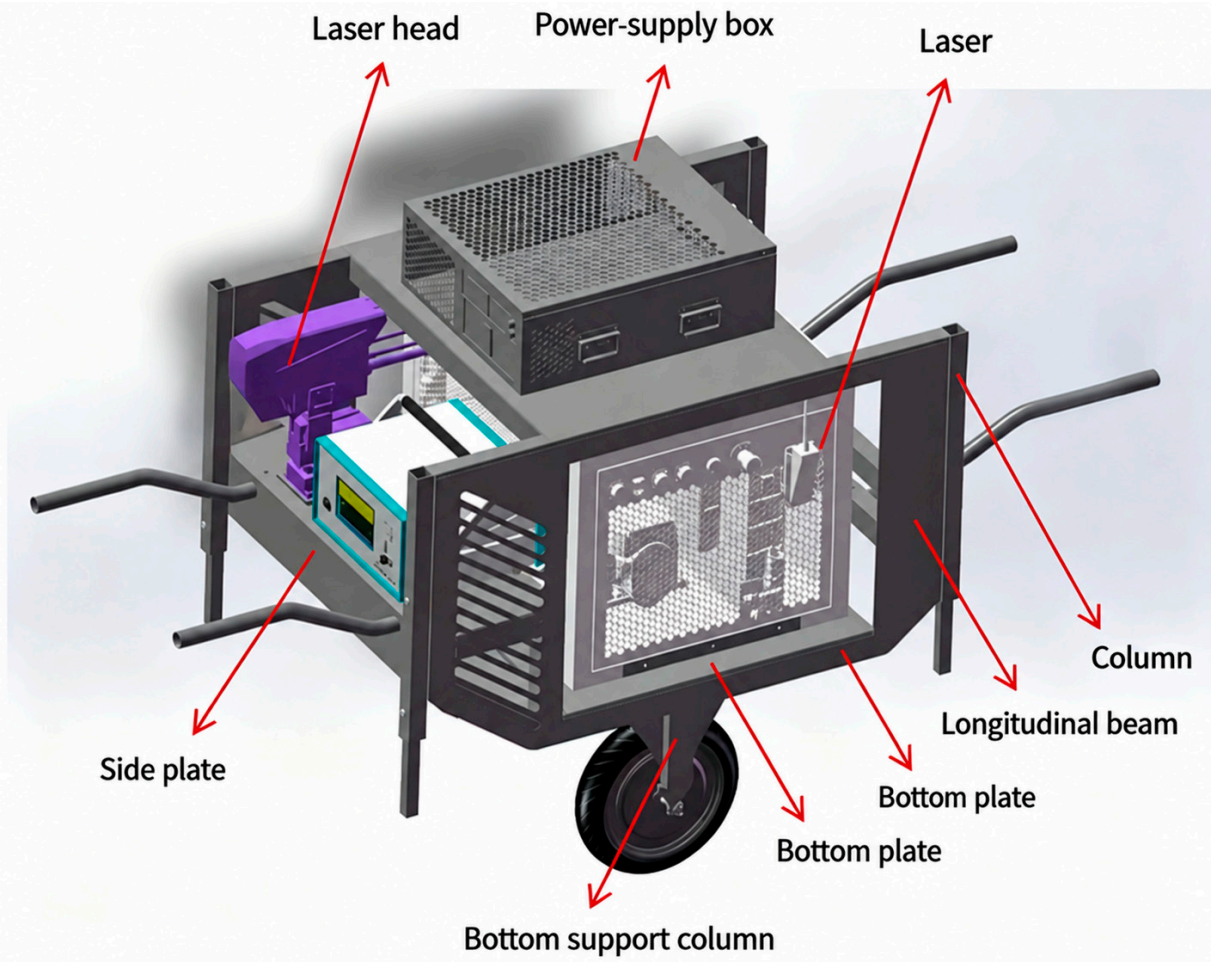


Figure 1. Structure of the vehicle-mounted laser emergency-response platform.

2.2. Mesh Generation and Sensitivity Assessment

Mesh sensitivity was evaluated using nominal global element sizes of 10, 8.0, and 6.4 mm. Following the reporting approach in [30], Table 1 lists the software-reported node and element counts together with the first six modal frequencies. Modal frequency was used as the primary dynamic metric. The mode index–frequency differences between the 8.0 and 6.4 mm meshes ranged from 0.35% to 4.61%, and the 8.0 mm mesh was selected as a balance between computational cost and frequency convergence.

Table 1. Dynamic mesh-sensitivity results based on the first six modal frequencies.

Metric	10 mm	8.0 mm (Retained)	6.4 mm	Difference: 8.0 vs. 6.4 mm (%)
Nodes	767,355	1,463,920	1,579,247	-
Elements	273,238	497,156	436,114	-
Mode 1 (Hz)	25.03	25.06	24.89	0.68
Mode 2 (Hz)	38.51	40.03	39.19	2.14
Mode 3 (Hz)	45.31	47.75	47.58	0.35
Mode 4 (Hz)	68.59	70.52	67.41	4.61
Mode 5 (Hz)	70.72	72.36	71.65	0.98
Mode 6 (Hz)	73.44	74.64	71.61	4.23

The final 8.0 mm model contained 1,463,920 nodes and 497,156 elements. Frequencies were paired by solver mode order because a modal assurance criterion (MAC) matrix was not available. Table 1 therefore indicates frequency convergence, while mode-shape correspondence requires a separate comparison.

2.3. Simulation Boundary Conditions

Two types of dynamic analysis were performed: modal analysis and random-vibration response analysis under multiple road conditions. The boundary conditions for each analysis were selected to represent the corresponding in-service constraint condition.

For the modal analysis, the transportation configuration was represented by linear translational springs at the wheel-mounting locations. Equivalent stiffnesses of 1.2×10^5 N/m in Z and 0.7×10^5 N/m in X and Y were estimated from the connection form, material properties, and structural dimensions of the wheel/support assembly using the linearized relation $k_i = F_i/\delta_i$. Rotational degrees of freedom were released, and no additional displacement constraints were applied. The estimated stiffnesses were used as equivalent support parameters for the present model.

For the random-vibration response analysis, the three directional auto-PSDs measured at the left-wheel support in each run were applied simultaneously at every wheel-support boundary. Support motions were represented as spatially uniform, fully coherent, and in phase within each direction, while the X, Y, and Z cross-spectral terms were treated as uncorrelated. The same support PSD was used at all supports within a run, and the measured run-specific PSDs were retained across the nine analyses. This equivalent uniform base-excitation model was adopted because only one support was instrumented; wheel-to-wheel phase differences, delays, coherence, and cross-spectral density could therefore not be evaluated.

2.4. Random-Vibration Analysis Parameters

The excitation, solution, and output parameters used in the multi-road-condition random-vibration analyses were matched to the road tests as follows.

2.4.1. Equivalent Excitation Parameters

Excitation source: Three repeated, synchronized three-axis acceleration records were available for each road condition. For every run, the left-wheel-support auto-PSDs were used as the common equivalent inputs at all FE wheel-support boundaries, while the laser-head-mount record was reserved for response comparison.

Time–frequency conversion and preprocessing: Every run contained 6661 synchronized samples acquired at 200 Hz, giving a record duration of 33.305 s. The acquisition export was in mm/s^2. The complete-record sample mean was removed for time-domain RMS calculation. For PSD estimation, each segment mean was removed; no additional linear detrending or post-acquisition digital filtering was applied. Welch averaging used

1024-sample Hann-windowed segments, 50% overlap (512 samples), no zero padding, one-sided density normalization by sampling frequency and window energy, and doubling of non-DC/non-Nyquist bins. Each run yielded 12 segments, and the three-run mean used 36 segments. The experimental frequency-bin spacing was 200/1024 = 0.1953125 Hz.

PSD averaging, uncertainty, and RMS definitions: The overlap-corrected effective degrees of freedom for the three-run mean PSD were approximately 68.54. The corresponding approximate pointwise 95% confidence limits were 0.734 and 1.442 times the estimated mean PSD. Component RMS values were calculated from each complete demeaned record. The three-axis resultant RMS was defined as $(RMS_x{}^2 + RMS_y{}^2 + RMS_z{}^2)^{(1/2)}$. Between-run variability is reported separately using the sample standard deviation and coefficient of variation (CV). PSD-integrated RMS and spectral comparisons excluded DC and used 0.1953125–80 Hz.

Analysis bandwidth: The 200 Hz sampling frequency gives a Nyquist frequency of 100 Hz. Quantitative comparisons were limited to 0.1953125–80 Hz because the modal solution extended to 78.911 Hz, and the spectral estimates near the Nyquist endpoint may be influenced by the acquisition-filter roll-off. The 80–100 Hz interval was therefore excluded from the model-error metrics. The acquisition anti-alias function was enabled, although its cutoff frequency, filter order, and roll-off were not retained and were treated as a source of measurement uncertainty.

Excitation unit: The acceleration power spectral density is expressed as $(mm^2/s^4)/Hz$.

2.4.2. Solution Parameters

Solution method: Modal superposition was performed using 20 extracted modes from 25.06 Hz to 78.911 Hz. At mode 20, the ANSYS participation-factor output gave cumulative effective-mass fractions of 0.999969, 0.999954, and 0.999958 in X, Y, and Z, respectively. Six selected mode shapes were displayed as Total Deformation results during post-processing. Because convergence beyond 20 modes was not evaluated, the response comparison was restricted to the retained 0–80 Hz band.

Sampling correspondence: The FE solver used a 0.1 Hz calculation step, whereas the experimental Welch bins were spaced by 0.1953125 Hz. FE spectra were therefore interpolated or matched to the experimental bins for comparison; 0.1 Hz was not described as the experimental resolution. Endpoint, leakage, and residual-alias effects were addressed by excluding DC and restricting quantitative comparison to 80 Hz.

Damping: A uniform modal damping ratio of 0.02 was assigned to the 20 retained modes as an engineering assumption for the lightly damped welded structure. No free-decay, half-power-bandwidth, or operational-modal damping identification was available. Operational-modal studies indicate that damping estimates are sensitive to the identification method and measurement conditions [31]. The road-response comparison therefore evaluates the combined effect of damping, support stiffness, contact representation, and input simplification rather than identifying the damping ratio independently.

2.4.3. Response Outputs

The observation location was the center of the laser-head mounting base. Two response metrics were extracted: component and three-axis resultant acceleration RMS values, in mm/s^2, calculated from the complete demeaned 33.305 s records; input and response acceleration PSDs, pointwise PSD confidence intervals, dominant spectral-peak frequencies, and wheel-input-to-laser-response magnitude-squared coherence over the 0.1953125–80 Hz comparison band.

3. Results

3.1. Modal Characteristics

Before the random-vibration response assessment, modal analysis was performed to identify the natural frequencies and mode shapes of the platform under the simulated transportation constraints. The linear free-vibration equation is

$$[M]\{\ddot{u}\} + [C]\{\dot{u}\} + [K]\{u\} = \{0\} \quad (1)$$

where [M] and [K] are the mass and stiffness matrices, respectively. The eigenvalue problem was solved using the Block Lanczos method. Figure 2 presents the first six mode shapes of the final 8 mm model using a consistent view and deformation scale.

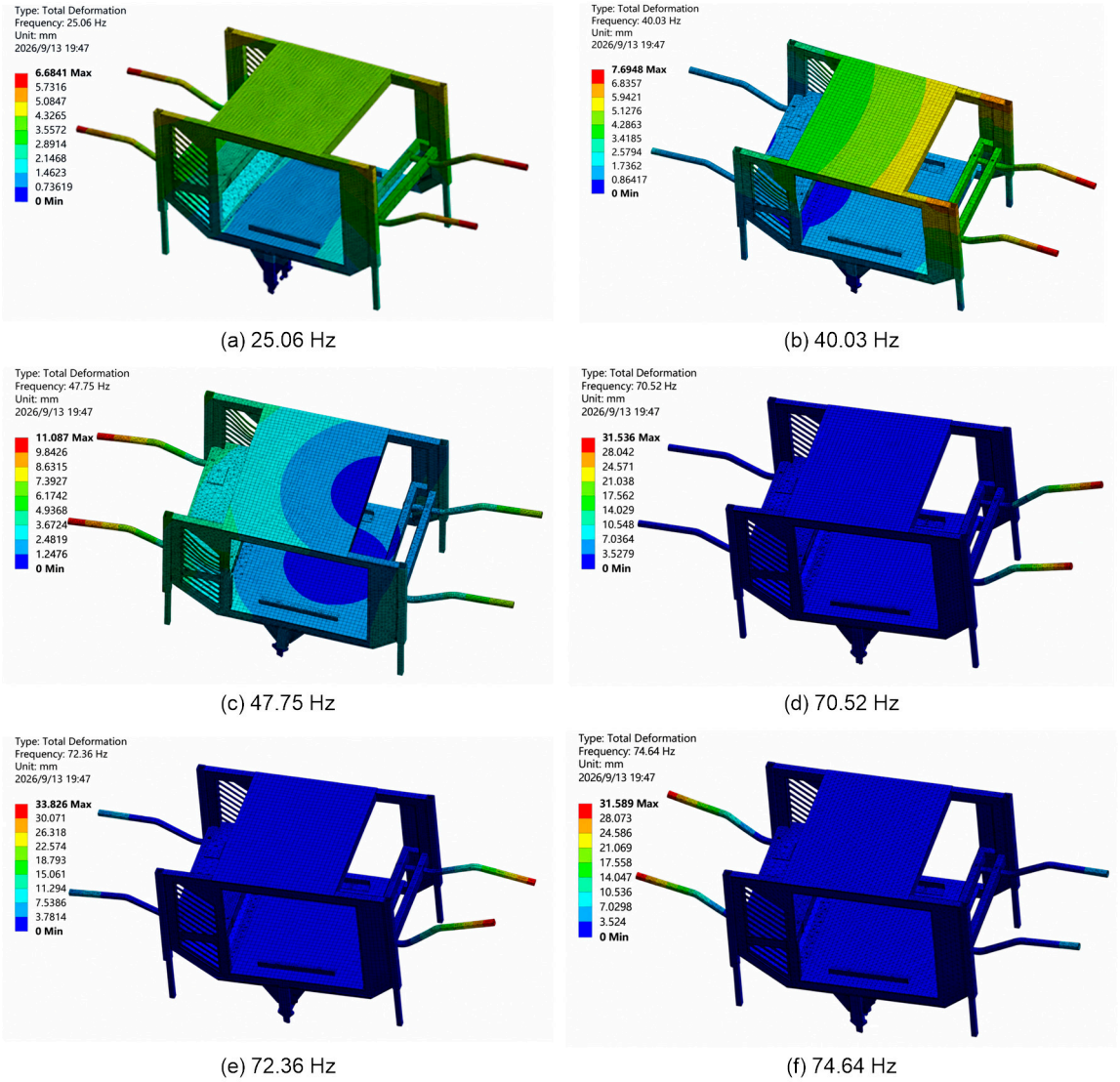


Figure 2. First six mode shapes of the retained 8 mm FE model.

The first six frequencies of the retained 8 mm mesh were 25.06, 40.03, 47.75, 70.52, 72.36, and 74.64 Hz. The subsequent random-vibration analysis used 20 modes and extended to 78.911 Hz. The cumulative effective-mass fractions exceeded 0.99995 in all three translational directions. In the absence of experimental modal data or an MAC matrix, these modal results provide a numerical basis for the response analysis rather than a direct experimental validation of the natural frequencies.

Natural frequencies and mode shapes describe the principal dynamic characteristics of a structure [4]. Differences between measured and calculated modal parameters can reveal modeling errors [5], and model-updating methods relate these differences to mass, stiffness, and connection parameters [6]. In this study, the modal analysis was used to examine the modeled mass and stiffness distribution and to provide a basis for the random-vibration solution.

In service, the platform is subjected to broadband road excitation, and its response amplitude depends not only on natural frequencies but also on damping, connection stiffness, and local structural characteristics. ASME V&V 10-2019 includes a comparison between computational predictions and experimental observations within the model-validation framework [7], while Oberkampf and Roy recommend selecting validation evidence according to the model's intended use [8]. The frequency-domain correlation approach of Pascual et al. indicates that response amplitudes and peak-frequency shifts can both be used to evaluate consistency between experimental and computational models [15]. Accordingly, the present assessment compares predicted and measured PSDs, resonance-peak locations, and response energy under measured road excitation.

3.2. Multi-Road-Condition Random-Vibration Tests

3.2.1. Experimental Rationale

Road tests were used to examine how closely the FE model reproduced the response amplitude and spectral characteristics measured at the laser-head mount. This system-level comparison reflects the combined effects of damping, support stiffness, contact representation, and excitation assumptions; the contribution of each parameter was not identified separately.

3.2.2. Test Setup

The road tests were conducted on flat asphalt, consecutive speed bumps, and damaged block-stone pavement. Two A322EX tri-axial acceleration nodes were installed: the input node at the left-wheel support and the response node at the center of the laser-head mounting base. Both nodes were fixed with screws. Three complete runs were recorded for each road condition and included in the statistical analysis. The measurement and analysis workflow is shown in Figure 3.

Three representative road conditions with different excitation characteristics were selected, as summarized in Table 2.

Table 2. Characteristics of the three road-test conditions.

Road Surface	Condition	Excitation Characteristics
Flat asphalt	Good	Primarily low-frequency excitation
Consecutive speed bumps	Periodic impacts	Distinct discrete-frequency components
Damaged block-stone road	Severe random excitation	Broadband distribution

The tests used two A322EX wireless tri-axial acceleration nodes manufactured by Beijing BeeTech Inc. (Beijing, China), as shown in Figure 4.

The principal specifications of the A322EX node are listed in Table 3.

The two measurement locations are shown in Figure 5. The input node recorded the local support acceleration used to construct the equivalent FE base input, and the response node recorded the acceleration at the laser-head mounting base. These were the only instrumented locations. The positive sensor axes are included in Figure 5 to show their correspondence with the FE coordinate system.

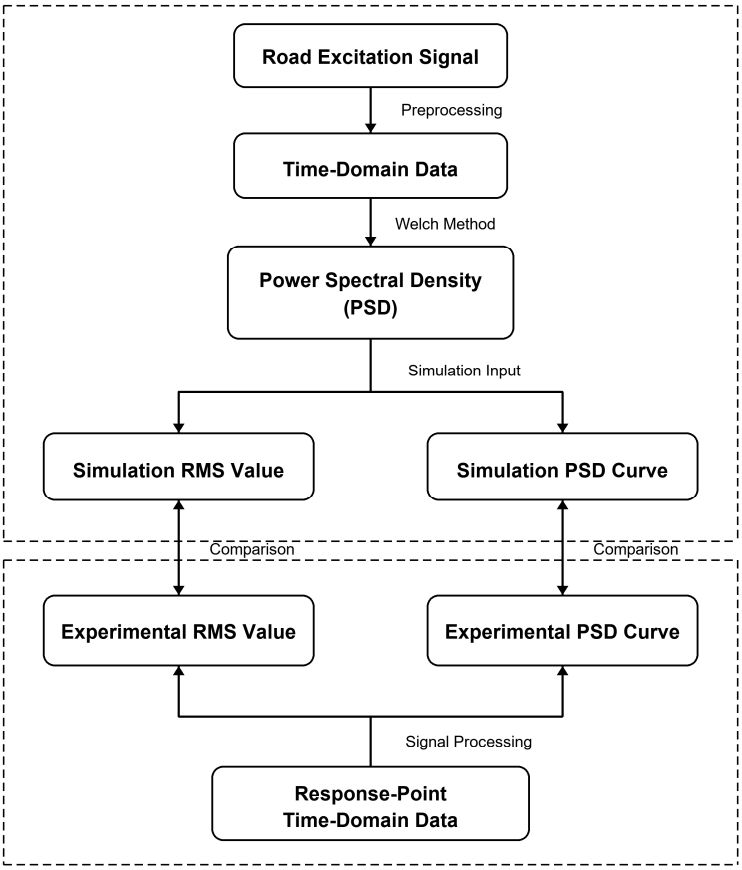


Figure 3. Workflow for the road-test-based FE model assessment.



Figure 4. A322EX wireless acceleration node.

Table 3. A322EX node specifications and measurement configuration.

Sensor/Test Characteristic	Value	Acquisition/Documentation Item	Value
Selected measurement range	±2 g	Sampling frequency	200 Hz
Measured axes	X, Y, Z	A/D resolution	12 bit
Frequency response (−3 dB)	300 Hz (X/Y); 150 Hz (Z)	Synchronization accuracy	0.1 ms
Measurement accuracy	6 mg at ±2 g	Nodes/channels	2/6
Input node	Left-wheel support	Response node	Laser-head mounting base
Mounting	Screw-fastened	Pre-run check	Zero-point check

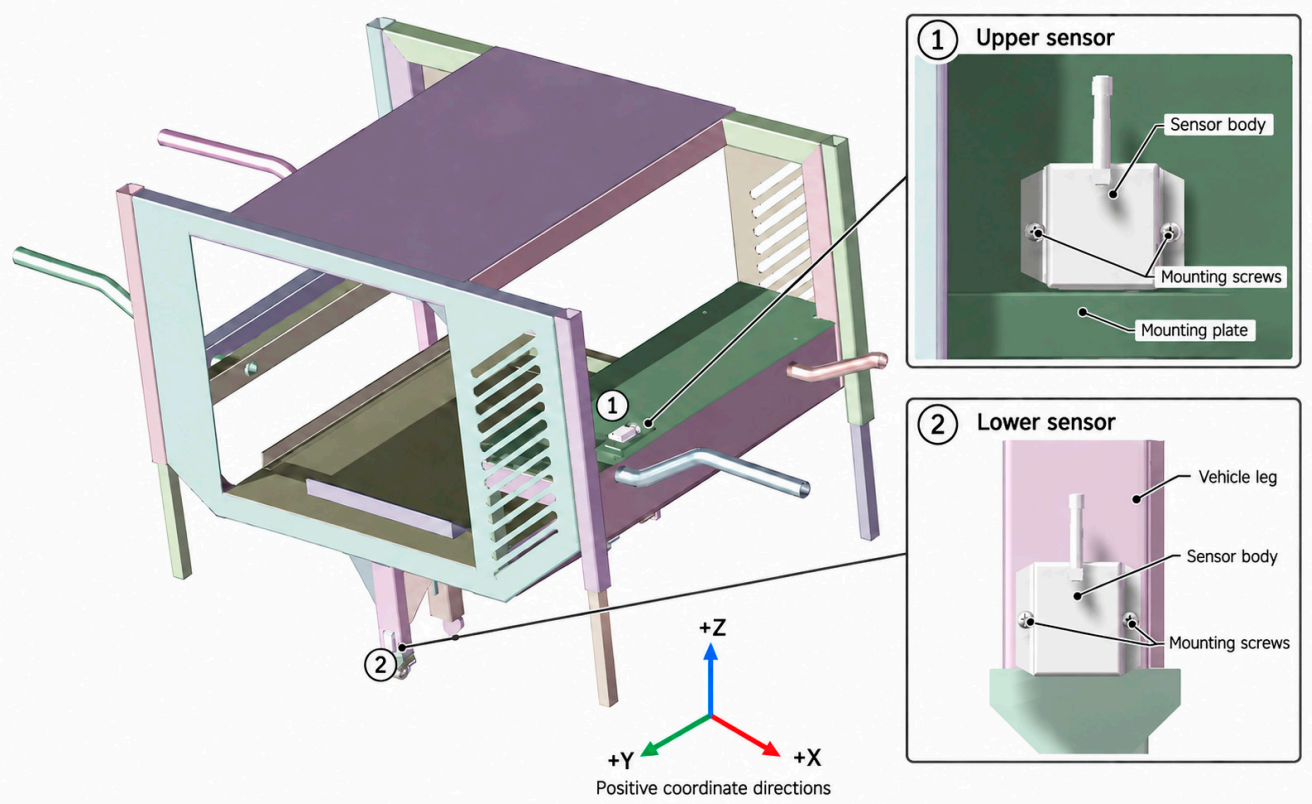


Figure 5. Sensor layout.

The selected measurement range was ±2 g. Before each run, a zero-point check was performed, and the acquisition anti-alias function was enabled. The sampling frequency was 200 Hz, and each record contained 6661 samples (33.305 s). Runs 1–3 were performed at 5.00, 4.93, and 5.07 km/h, corresponding to effective travel distances of 46.25, 45.60, and 46.90 m; the nominal road section was approximately 45 m. Tests were conducted under normal ambient conditions. All three complete records were used for quantitative analysis. For time-history visualization only, Run 1 was selected because its resultant RMS was closest to the corresponding three-run mean, providing an objective representative-signal criterion consistent with recent road-vibration reporting practice [23].

Before each run, the two screw-mounted accelerometers were subjected to a zero-offset check. The manufacturer-reported measurement accuracy of 6 mg at the selected ±2 g range was therefore used to characterize instrument accuracy. The acquisition anti-alias function was enabled, although its cutoff frequency, filter order, and roll-off characteristics were not recorded. The tests were conducted under normal ambient conditions, but temperature and relative humidity were not logged. These factors were considered when interpreting the experimental uncertainty.

3.2.3. Experimental Results

Figures 6–10 summarize the measured time histories and frequency-domain response comparisons for the three roads and three axes. Figure 6 presents the synchronized measured input and response time histories. Figure 7 compares the input, measured-response, and FE-response PSDs with uncertainty bands for the measured-response estimates. Figures 8–10 present measured input–response coherence, H1 acceleration transmissibility, and locally matched measured and FE spectral peaks. The coherence characterizes the measured wheel-support-to-laser-mount path; spatial coherence among the wheel supports was not measured.

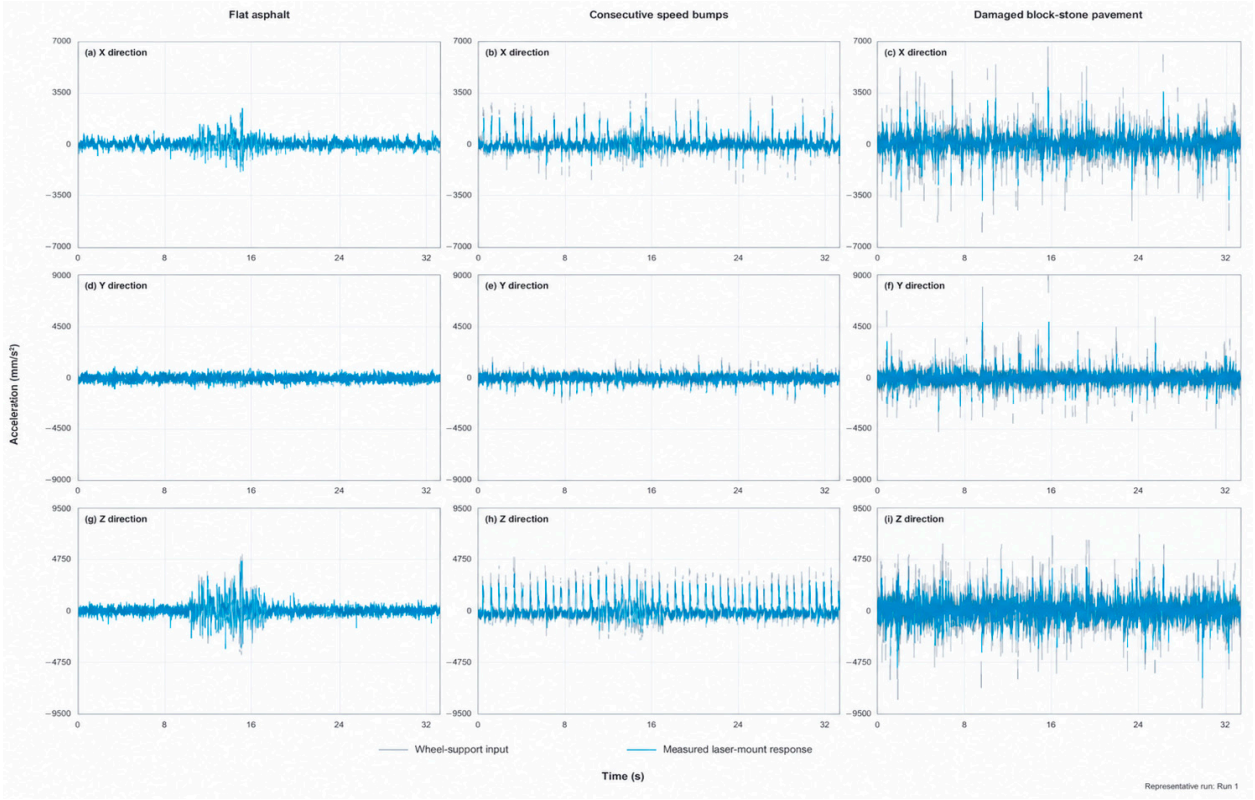


Figure 6. Axis-specific left-wheel input and measured laser-head-mount response.

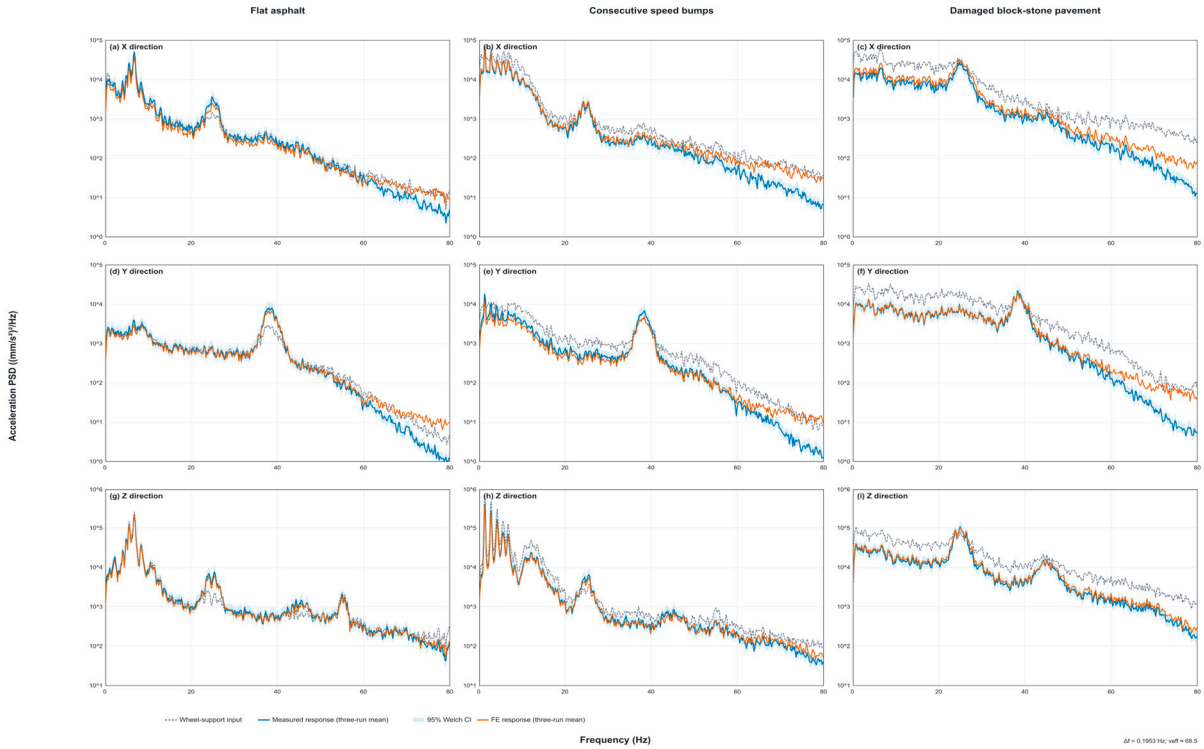


Figure 7. Three-run mean input, measured-response, and FE-response PSDs for all road-axis combinations. Shading denotes the approximate pointwise 95% confidence interval of the three-run mean measured-response PSD; comparison is restricted to 0.1953125–80 Hz.

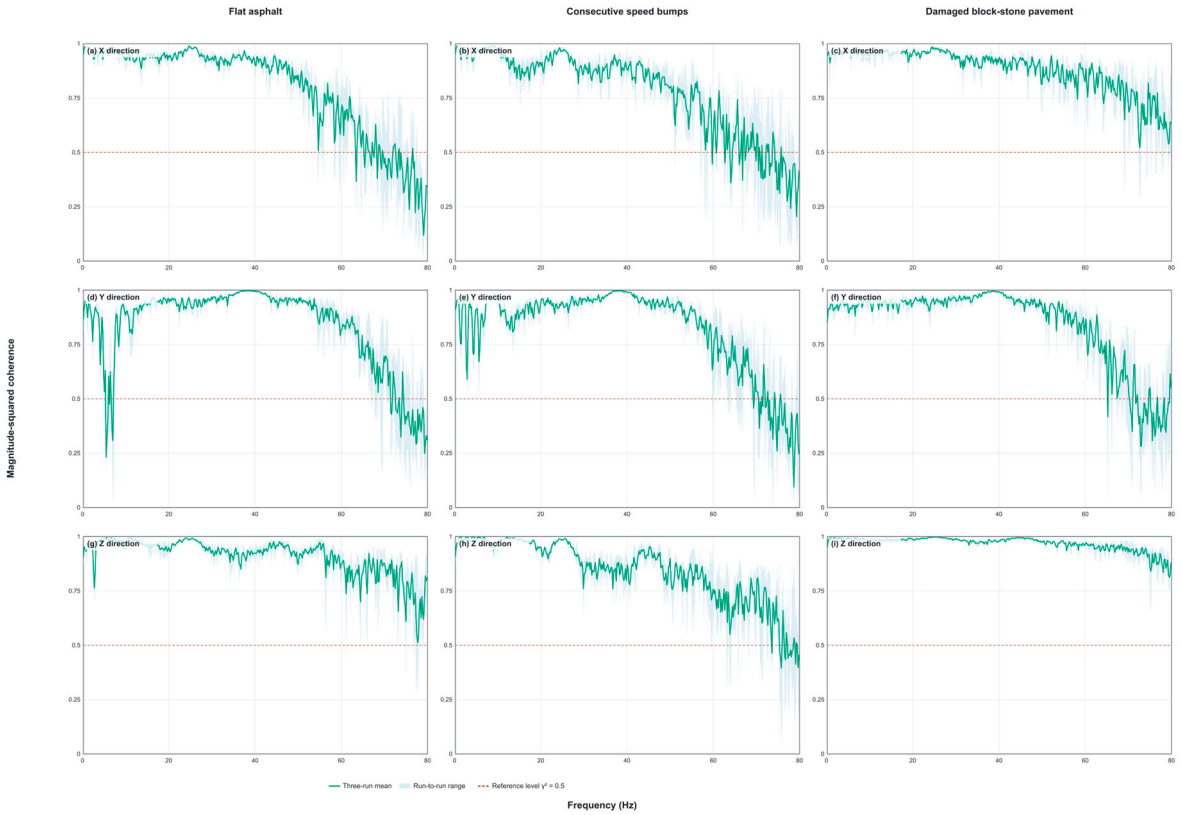


Figure 8. Three-run mean magnitude-squared coherence between the measured left-wheel-support input and laser-head-mount response for all road-axis combinations.

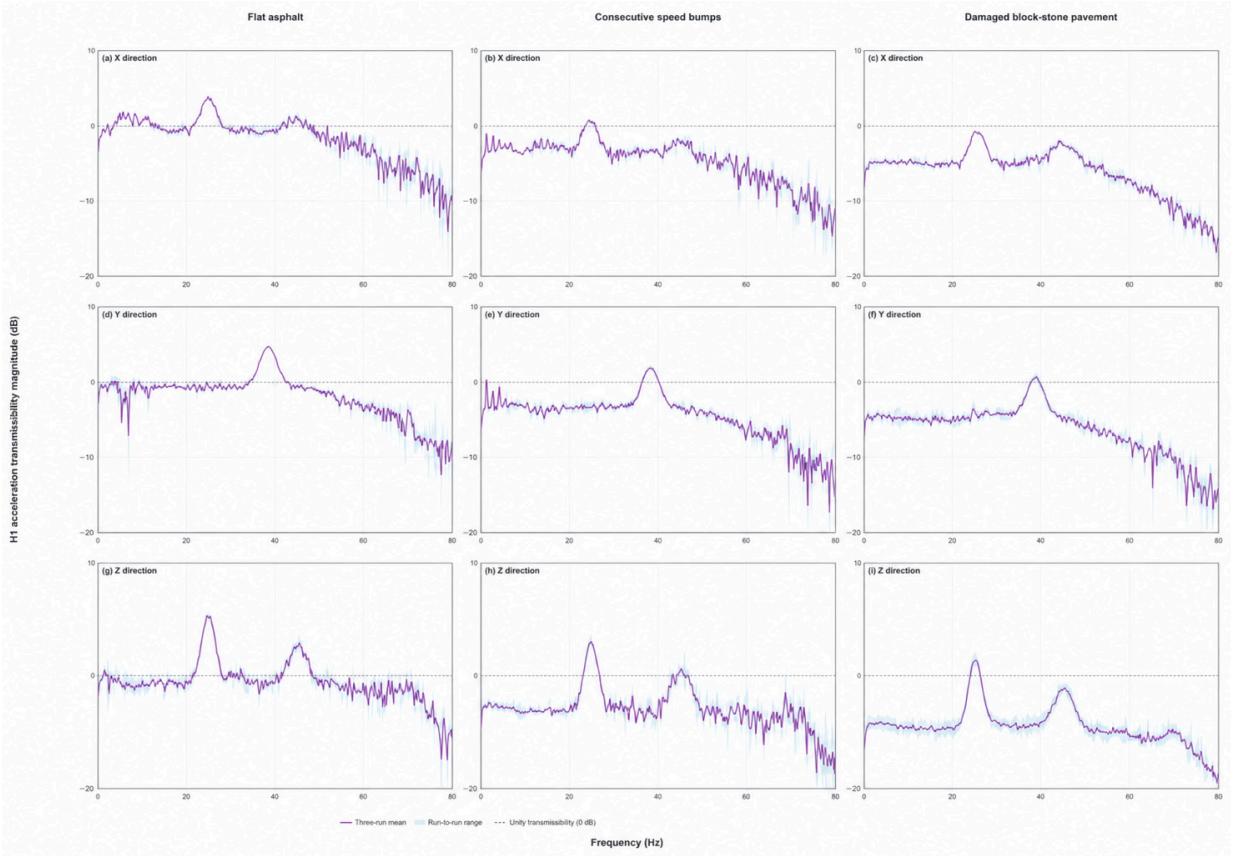


Figure 9. Three-run mean H_1 acceleration transmissibility from the measured left-wheel support to the laser-head mounting base, with between-run variability shown in decibels.

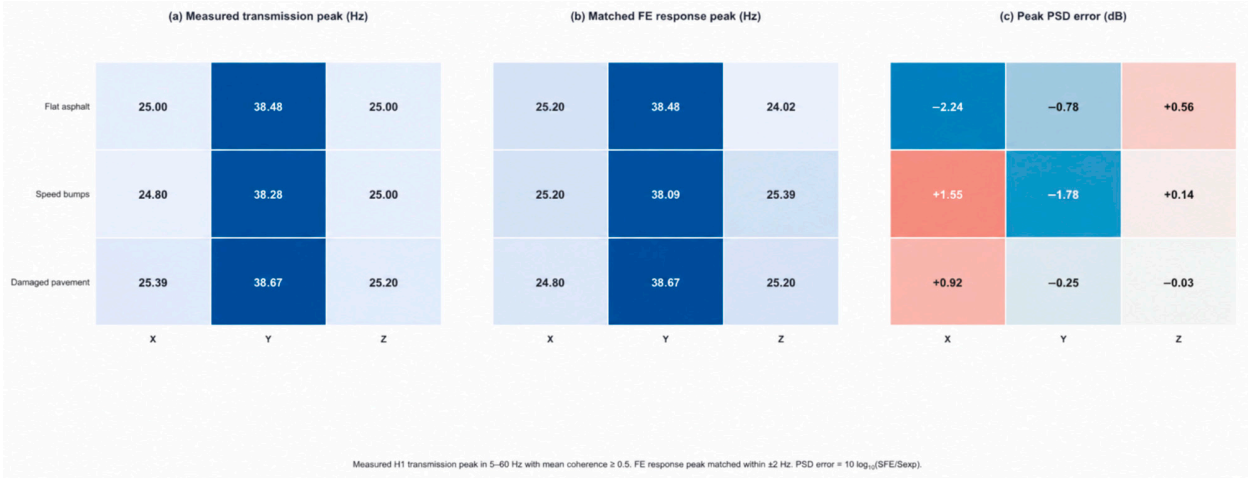


Figure 10. Dominant measured H_1 transmission-resonance candidates and locally matched FE peaks.

Table 4 summarizes the three-run mean and sample standard deviation of the measured and FE RMS values. The signed errors in the mean three-axis resultant RMS were −4.54%, −3.58%, and +6.43% for flat asphalt, consecutive speed bumps, and damaged block-stone pavement, respectively, giving a mean absolute error of approximately 4.85%. The largest axis-specific mean error was +13.73% for the damaged-road X response. Measured resultant–RMS CVs were 1.55%, 1.37%, and 2.40%, indicating modest but non-negligible stochastic run-to-run variability.

Table 4. Three-run measured and FE acceleration RMS statistics at the laser-head mounting location.

Road	Component	Measured Mean	Measured SD	FE Mean	FE SD	Signed Error (%)
Flat asphalt	X	350.806	7.821	304.459	0.530	−13.21
Flat asphalt	Y	262.157	7.006	249.374	10.472	−4.88
Flat asphalt	Z	606.264	16.721	595.758	7.039	−1.73
Flat asphalt	Resultant	748.009	11.592	714.049	8.641	−4.54
Speed bumps	X	480.424	12.552	495.367	35.119	+3.11
Speed bumps	Y	313.899	8.578	273.047	13.938	−13.02
Speed bumps	Z	769.095	12.265	731.776	3.950	−4.85
Speed bumps	Resultant	959.680	13.154	925.324	16.263	−3.58
Damaged road	X	584.558	19.123	664.800	14.758	+13.73
Damaged road	Y	531.364	37.885	541.596	48.465	+1.93
Damaged road	Z	947.273	23.346	994.019	12.302	+4.94
Damaged road	Resultant	1233.840	29.612	1313.169	33.713	+6.43

The mean logarithmic PSD correlation coefficient over 0–80 Hz was approximately 0.979 across the road-axis comparisons. As shown in Table 5, the measured H_1 resonance peaks occurred near 25 Hz in X/Z and near 38.3–38.7 Hz in Y. The corresponding FE frequency differences ranged from −0.98 to +0.39 Hz. Peak-PSD differences ranged from −2.24 to +1.55 dB, and coherence at the measured peaks ranged from 0.966 to 0.998. The close peak-frequency agreement indicates that the model captured the dominant transmission frequencies, while the remaining amplitude differences varied with road condition and direction.

Table 5. Dominant measured H_1 transmission peaks, locally matched FE peaks, and peak coherence.

Road	Axis	Exp. Peak (Hz)	FE Peak (Hz)	Δf (Hz)	Peak PSD Error (dB)	Coherence
Flat asphalt	X	25.000	25.195	+0.195	−2.24	0.981
Flat asphalt	Y	38.477	38.477	0.000	−0.78	0.997

Table 5. *Cont.*

Road	Axis	Exp. Peak (Hz)	FE Peak (Hz)	Δf (Hz)	Peak PSD Error (dB)	Coherence
Flat asphalt	Z	25.000	24.023	−0.977	+0.56	0.988
Speed bumps	X	24.805	25.195	+0.391	+1.55	0.966
Speed bumps	Y	38.281	38.086	−0.195	−1.78	0.997
Speed bumps	Z	25.000	25.391	+0.391	+0.14	0.986
Damaged road	X	25.391	24.805	−0.586	+0.92	0.980
Damaged road	Y	38.672	38.672	0.000	−0.25	0.995
Damaged road	Z	25.195	25.195	0.000	−0.03	0.998

4. Discussion

The repeated-road comparison provides a system-level assessment of the vehicle-mounted laser platform under measured operating excitation. Across the three road conditions, the FE results reproduced the overall response energy with a mean absolute resultant–RMS error of 4.85% and reproduced the logarithmic PSD shape with an average correlation of approximately 0.979. Agreement was strongest for the Z-direction RMS on flat asphalt and for the resonance frequencies in Table 5. The largest component-level differences occurred in the damaged-road X response and the speed-bump Y response, suggesting that broadband energy and dominant transmission frequencies were reproduced more consistently than individual directional amplitudes.

The three repeated runs were used to quantify the variability of the road response. The measured resultant–RMS CVs ranged from 1.37% to 2.40%, and the corresponding 95% confidence intervals for the mean resultant RMS were 719.2–776.8, 927.0–992.4, and 1160.3–1307.4 mm/s^2 for flat asphalt, speed bumps, and damaged road, respectively. Axis-specific variability was higher in some cases and reached approximately 7.13% for the damaged-road Y response. Model differences of a few percent should therefore be considered together with the observed run-to-run variability.

The input representation is the main limitation of the present model. Identical auto-PSDs were applied at every support with full within-direction coherence, zero phase difference, and no cross-axis spectral terms. This representation is consistent with the available single-support measurement, but it does not include axle delays, left–right differences, wheel–path asymmetries, or cross-direction coupling. Future measurements with synchronized tri-axial sensors at all supports would allow for the frequency-dependent cross-spectral density matrix to be included [19].

The 2% modal damping ratio and equivalent support stiffnesses were used as combined engineering inputs. Because these parameters were not identified separately, different parameter combinations may produce similar RMS and PSD responses. The road tests support the overall response of the model under the selected parameters. Independent estimates would require damping identification from free-decay or operational-modal data and direct measurement of support compliance.

The dynamic mesh comparison supports the use of the 8 mm mesh on the basis of the first six modal frequencies. The 20-mode basis captures more than 99.995% of the cumulative translational effective mass and extends to 78.911 Hz. Further work should confirm mode-shape pairing between meshes and compare the response PSD, resonance frequencies, and integrated RMS obtained with 20 and higher modal truncations. The present model is therefore used for comparative assessment within the tested 0–80 Hz range.

The results apply to the tested platform and mass configuration, the two measurement locations, the three road classes, an operating speed of approximately 5 km/h, a nominal 45 m road section, the selected boundary parameters, and the 0–80 Hz comparison band. Within these conditions, the workflow can support comparisons of mounting layouts and

vibration-mitigation measures. Application to other vehicles, speeds, payloads, road surfaces, or support-correlation conditions requires additional measurements. The 200 Hz sampling frequency provides a 100 Hz Nyquist limit, while the 1024-point Welch segments provide a resolution of 0.1953125 Hz. The unavailable anti-alias filter characteristics remain part of the measurement uncertainty. Table 6 summarizes the differences between conventional modal testing and the present workflow.

Table 6. Comparison of conventional modal testing and the present repeated-road response-assessment workflow.

Comparison Criterion	Conventional Modal Testing	Present Workflow
Excitation	Artificial excitation (impact hammer/shaker)	Repeated measured road input represented as common equivalent support PSDs
Assessment metrics	Natural frequencies and mode shapes	Modal frequencies, axis-specific time histories, PSDs, coherence, transmissibility, RMS, and uncertainty
Boundary conditions	Simplified (free/fixed)	Approximate in-service springs and contact idealizations
Applicable structures	Small or medium, relatively simple structures	Demonstrated for one platform and the stated test envelope
Experimental cost	High (excitation equipment and many sensors)	Two tri-axial nodes and three repeated runs per road
Integration with design workflow	Indirect	Direct for comparative design under retained assumptions

5. Conclusions

This study combined FE random-vibration analysis with repeated road measurements to assess the response of a vehicle-mounted laser platform. The workflow integrates dynamic mesh sensitivity, a documented 20-mode basis, repeated three-axis measurements, spectral uncertainty, and axis-specific response metrics at the laser-head mounting base. The main conclusions are as follows:

(1) The retained 8 mm mesh gave first-six modal frequencies of 25.06, 40.03, 47.75, 70.52, 72.36, and 74.64 Hz. The random-vibration analysis used 20 modes through 78.911 Hz, with cumulative translational effective-mass fractions above 0.99995. These results support frequency convergence of the selected mesh; mode-shape pairing and higher-mode response convergence require further study.

(2) For the three road conditions, the mean absolute error in the three-axis resultant RMS was approximately 4.85%, and the mean logarithmic PSD correlation over 0-80 Hz was approximately 0.979. The measured resultant–RMS CVs ranged from 1.37% to 2.40%. Dominant transmission peaks were matched within −0.98 to +0.39 Hz, although the directional amplitude agreement varied among the road conditions.

(3) The workflow is suitable for comparative studies of vibration mitigation, support stiffness, and mounting layout for the tested platform under similar road and speed conditions. Using repeatability, uncertainty bands, coherence, peak differences, and RMS together provides a broader assessment of model agreement than RMS alone.

(4) The current assessment is influenced by the single-support input measurement, uniform coherent support excitation, assumed 2% damping ratio, estimated support stiffnesses, idealized contacts, incomplete calibration and anti-alias metadata, and the limited test envelope. The experiments assess the combined system response under these assumptions. Future work will focus on multi-support measurements; independent identification of damping and support compliance; modal and response

convergence; and tests covering additional speeds, payloads, platforms, and environmental conditions.

Author Contributions: Y.X. Writing—original draft, J.W. Project administration, J.C. Data curation, H.Z. Supervision and G.H. Writing—review and editing. All authors have read and agreed to the published version of the manuscript.

Funding: This research was funded by the National Key Research and Development Program of China, grant number 2023YFC3010904.

Data Availability Statement: The original contributions presented in this study are included in the article. Further inquiries can be directed to the corresponding authors.

Conflicts of Interest: Author Jingang Wang was employed by the company Sunward Intelligent Special Equipment Co., Ltd. The remaining authors declare that the research was conducted in the absence of any commercial or financial relationships that could be construed as a potential conflict of interest.

References

1. Periu, C.F.; Mohsenimanesh, A.; Laguë, C.; McLaughlin, N.B. Isolation of vibrations transmitted to a LIDAR sensor mounted on an agricultural vehicle to improve obstacle detection. *Can. Biosyst. Eng.* **2013**, *55*, 2.33–2.42. [CrossRef]
2. Schlager, B.; Goelles, T.; Behmer, M.; Muckenhuber, S.; Payer, J.; Watzenig, D. Automotive lidar and vibration: Resonance, inertial measurement unit, and effects on the point cloud. *IEEE Open J. Intell. Transp. Syst.* **2022**, *3*, 426–434. [CrossRef]
3. Hua, Y.; Wang, S.; Li, B.; Bai, G.; Zhang, P. Dynamic modeling and anti-disturbing control of an electromagnetic MEMS torsional micromirror considering external vibrations in vehicular LiDAR. *Micromachines* **2021**, *12*, 69. [CrossRef] [PubMed]
4. Ewins, D.J. *Modal Testing: Theory, Practice and Application*, 2nd ed.; Research Studies Press: Baldock, UK, 2000.
5. Mottershead, J.E.; Friswell, M.I. Model updating in structural dynamics: A survey. *J. Sound Vib.* **1993**, *167*, 347–375. [CrossRef]
6. Friswell, M.I.; Mottershead, J.E. *Finite Element Model Updating in Structural Dynamics*; Kluwer Academic Publishers: Dordrecht, The Netherlands, 1995. [CrossRef]
7. American Society of Mechanical Engineers. *ASME V&V 10-2019: Standard for Verification and Validation in Computational Solid Mechanics*; ASME: New York, NY, USA, 2019.
8. Oberkampf, W.L.; Roy, C.J. *Verification and Validation in Scientific Computing*; Cambridge University Press: Cambridge, UK, 2010. [CrossRef]
9. Allemang, R.J. The modal assurance criterion-twenty years of use and abuse. *Sound Vib.* **2003**, *37*, 14–23.
10. Reynders, E. System identification methods for (operational) modal analysis: Review and comparison. *Arch. Comput. Methods Eng.* **2012**, *19*, 51–124. [CrossRef]
11. Peeters, B.; De Roeck, G. Stochastic system identification for operational modal analysis: A review. *J. Dyn. Syst. Meas. Control* **2001**, *123*, 659–667. [CrossRef]
12. Welch, P.D. The use of fast Fourier transform for the estimation of power spectra: A method based on time averaging over short, modified periodograms. *IEEE Trans. Audio Electroacoust.* **1967**, *15*, 70–73. [CrossRef]
13. Bendat, J.S.; Piersol, A.G. *Random Data: Analysis and Measurement Procedures*, 4th ed.; John Wiley & Sons: Hoboken, NJ, USA, 2010. [CrossRef]
14. *ISO 8608:2016*; Mechanical Vibration-Road Surface Profiles-Reporting of Measured Data, 2nd ed. International Organization for Standardization: Geneva, Switzerland, 2016.
15. Pascual, R.; Golinval, J.C.; Razeto, M. A frequency domain correlation technique for model correlation and updating. In Proceedings of the 15th International Modal Analysis Conference, Orlando, FL, USA, 3–6 February 1997; pp. 587–592.
16. Mottershead, J.E.; Link, M.; Friswell, M.I. The sensitivity method in finite element model updating: A tutorial. *Mech. Syst. Signal Process.* **2010**, *25*, 2275–2296, Erratum in *Mech. Syst. Signal Process* **2011**, *25*, 2275–2296. [CrossRef]
17. Martins, L.; Romero, G.; Suarez, B. Enhancing the accuracy of linear finite element models of vehicle structures considering spot-welded flanges. *Materials* **2021**, *14*, 6075. [CrossRef] [PubMed]
18. Shrivastava, K.; Vijayan, K.; Arora, V. Experimental identification of dynamic characteristics of welded stiffened structures based on model updating. *Thin-Walled Struct.* **2023**, *184*, 110485. [CrossRef]
19. Talik, S.; Claeys, M.; Sinou, J.-J.; Lambelin, J.-P. Random vibration analysis under correlated multi-point excitation. *Eur. J. Mech. A/Solids* **2022**, *96*, 104769. [CrossRef]
20. Martini, A.; Bonelli, G.P.; Rivola, A. Virtual testing of counterbalance forklift trucks: Implementation and experimental validation of a numerical multibody model. *Machines* **2020**, *8*, 26. [CrossRef]

21. Rapino, L.; La Paglia, I.; Ripamonti, F.; Corradi, R.; Di Lione, R.; Baro, S. Measurement and processing of road irregularity for surface generation and tyre dynamics simulation in NVH context. *Int. J. Pavement Res. Technol.* **2024**, *17*, 918–928. [CrossRef]
22. Tonelli, R.; Buckert, S.; Patrucco, A.; Bragado Perez, B.; Gutierrez, J.; Sanchez, A. Electric vehicle ride and vibrations analysis: Full electric vehicle MBD model development for NVH studies. *SAE Int. J. Adv. Curr. Pract. Mobil.* **2025**, *7*, 1024–1034. [CrossRef]
23. Karpenko, M.; Prentkovskis, O.; Skačkauskas, P. Analysing the impact of electric kick-scooters on drivers: Vibration and frequency transmission during the ride on different types of urban pavements. *Eksploat. Niezawodn. Maint. Reliab.* **2025**, *27*, 199893. [CrossRef]
24. Karpenko, M.; Ževžikov, P.; Stosiak, M.; Skačkauskas, P.; Borucka, A.; Delembovskyi, M. Vibration research on centrifugal loop dryer machines used in plastic recycling processes. *Machines* **2024**, *12*, 29. [CrossRef]
25. Zhu, Z.; Meng, Q. Analysis on random vibration and impact response of vehicle-borne electronic chassis. In *Proceedings of the 8th International Conference on Advances in Construction Machinery and Vehicle Engineering*; Springer: Singapore, 2024; pp. 1281–1296. [CrossRef]
26. Campello, L.; Denis, V.; Sesana, R.; Delprete, C.; Serra, R. New experimental single-axis excitation set-up for multi-axial random fatigue assessments. *Machines* **2025**, *13*, 539. [CrossRef]
27. Xie, Y.; Xue, Y.; Wang, H.; Sun, Y. Structural design and random vibration analysis of a high-stability momentum wheel. *Machines* **2025**, *13*, 406. [CrossRef]
28. Kaliorakis, N.; Sakellariou, J.S.; Fassois, S.D. On-board random vibration-based robust detection of railway hollow worn wheels under varying traveling speeds. *Machines* **2023**, *11*, 933. [CrossRef]
29. Kim, C.J. Accelerated sine-on-random vibration test method of ground vehicle components over conventional single mode excitation. *Appl. Sci.* **2017**, *7*, 805. [CrossRef]
30. Karpenko, M. Aircraft hydraulic drive energy losses and operation delay associated with pipeline/fitting connections. *Aviation* **2024**, *28*, 1–8. [CrossRef]
31. Kudu, F.N.; Uçak, Ş.; Osmancikli, G.; Türker, T.; Bayraktar, A. Estimation of damping ratios of steel structures by operational modal analysis method. *J. Constr. Steel Res.* **2015**, *112*, 61–68. [CrossRef]

Disclaimer/Publisher's Note: The statements, opinions and data contained in all publications are solely those of the individual author(s) and contributor(s) and not of MDPI and/or the editor(s). MDPI and/or the editor(s) disclaim responsibility for any injury to people or property resulting from any ideas, methods, instructions or products referred to in the content.